Chapter 8

Noise of *pn* Junction Lasers and Detectors

In this chapter we will review the noise properties of two important *pn* junction devices: semiconductor lasers and avalanche photodiodes. Two remarkable results will be presented. A first striking results is that the shot noise can be suppressed in a semiconductor laser driven by a high-impedance constant current source [1, 2]. A second important result is that the excess noise can be suppressed in an avalanche photodiode driven by a low *dc* field [3, 4]

8.1 Amplitude Squeezing in Semiconductor Lasers

8.1.1 Noise equivalent circuit of a semiconductor laser

The following facts are discovered by the microscopic theory for carrier transport and radiative recombination in *pn* junctions presented in Chapter 6.

1. The shot-noise-limited current noise in a *pn* junction diode is not the noise introduced by the pump source, but is the result of the thermal fluctuation of minority carrier flow (diffusion noise) and generation-recombination noise inside the diode.

2. This shot-noise-limited current noise exists only when the diode is biased by a constant-voltage source (negligible source resistance).

3. The pump noise for a semiconductor laser is the Johnson-Nyquist (thermal) noise generated in the source resistance. In the strong forward-bias condition, the diode's differential resistance becomes smaller than the source resistance, and in such a case the (thermal) pump noise becomes smaller than the shot-noise level (high-impedance suppression).

We can now construct a complete and self-consistent noise-equivalent circuit for a semiconductor laser, including the mutual coupling between the pump source and the junction.

The noise-equivalent circuit shown in Fig. 8.1 consists of the four parts[5]: pump (input electron flux) fluctuation, population inversion (internal electron number) fluctuation, internal photon-number fluctuation, and output photon flux fluctuation, respectively.

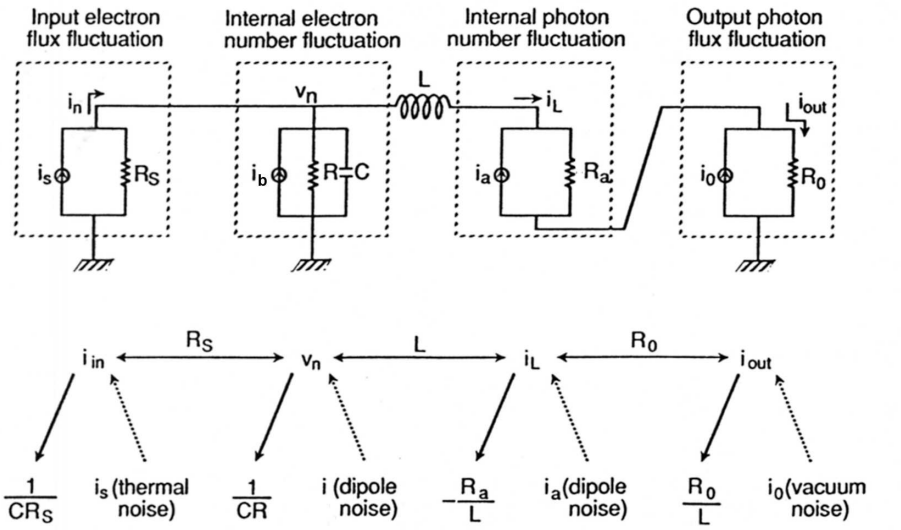

Figure 8.1: Noise-equivalent circuit of a semiconductor laser and the dissipation-fluctuation relations.

Electron number fluctuation ΔN_c is uniquely determined by junction-voltage fluctuation υ_n via $\frac{\Delta N_c}{N_c} = \frac{\upsilon_n}{2V_T}$, where $V_T = \frac{k_B T}{q}$ is a thermal voltage. Thus, the electron-number fluctuation inside the active region corresponds to the fluctuation of the charge stored in capacitance C in Fig. 8.1. Electron-number fluctuation ΔN_c has two decay processes, one via source resistance R_S and the other via differential resistance R. The circuit equation for the first process (assuming $R \to \infty$ and $i \to 0$) is

$$\left(\frac{1}{R_S} + i\omega C\right) = i_s \quad , \tag{8.1}$$

or equivalently

$$\frac{d}{dt}\Delta N_c = -\frac{1}{CR_S}\Delta N_c + \frac{i_s}{q} \quad . \tag{8.2}$$

The power spectral density of the noise source $\frac{i_s}{q}$,

$$S_{i_s/q}(\omega) = \frac{4k_B T}{q^2 R_S} = 2\frac{N_c}{CR_S} \quad , \tag{8.3}$$

is equal to twice of the electron-number decay rate via the source resistance. This is the fluctuation-dissipation theorem for the CR_S decay process. The pump source functions to restore the electron number to its average value. This relaxation process with decay rate $\frac{1}{CR_S}$ accompanies noise Eq. (8.3), which is the origin of the pump noise for a semiconductor laser. The noise current is the thermal noise of the source resistance, since $\hbar\omega \ll k_B T$.

The circuit equation for the second process (assuming $R_S \to \infty$ and $i_s \to 0$) is

$$\left(\frac{1}{R} + i\omega C\right) \upsilon_n = i_b \quad , \tag{8.4}$$

or equivalently

$$\frac{d}{dt}\Delta N_c = -\frac{1}{CR}\Delta N_c + \frac{i_b}{q} \quad . \tag{8.5}$$

As expected, decay rate $\frac{1}{CR}$ is equal to the inverse of effective electron lifetime $\frac{1}{\tau_n} = \left(\frac{1}{\tau_{\rm nr}} + \frac{1}{\tau_{\rm sp}} + \frac{1}{\tau_{\rm st}}\right)$, indicating that the second process is the relaxation process of the electron number fluctuation due to internal radiative and nonradiative recombination. The power spectral density of the noise source $\frac{i_b}{q}$,

$$S_{i_b/q}(\omega) = 2\left[\frac{N_c}{CR} + 2E_{vc}S_0\right] \quad , \tag{8.6}$$

is equal to twice of the electron-number decay rate via the differential resistance (full-shot noise), plus a stimulated absorption term. This is the fluctuation-dissipation theorem for the CR decay process. The origin of this noise current is dipole moment noise source, which will be discussed in Chapter 10. Combining Eqs. (8.2) and (8.5) gives

$$\frac{d}{dt}\Delta N_c = -\left(\frac{1}{CR_S} + \frac{1}{\tau_n}\right)\Delta N_c + \frac{1}{q}\left(i_s + i_b\right) \quad . \tag{8.7}$$

The average junction current carried by the lasing photons is $I_L = q\gamma S_0$. The photon-number fluctuation is thus determined by photon current fluctuation i_L via $\Delta S = \frac{i_L}{q\gamma}$. The photon-number fluctuation inside the active region is proportional to the fluctuation of the current flowing in inductance L in Fig. 8.1. We assume that the electron energy is stored in capacitance C, that the photon energy is stored in inductance $L = \tau_{\rm st}/C\gamma$, and that $\omega_r \equiv 1/\sqrt{LC} = \sqrt{\gamma/\tau_{st}}$ is the relaxation oscillation frequency. Current fluctuation i_L is amplified by negative resistance $-R_a$ (stimulated emission gain) and is attenuated by positive resistance R_0 (output coupling loss). The circuit equation for the first process (assuming $R_0 \to 0$) is

$$(i\omega L - R_a)i_L = R_a i_a \quad , \tag{8.8}$$

or equivalently

$$\frac{d}{dt}\Delta S = \frac{R_a}{L}\Delta S + \frac{i_a}{q} \quad . \tag{8.9}$$

Here, the relation $\frac{R_a}{L} = E_{cv} - E_{vc} \simeq \gamma$ is used. The power spectral density of the noise source $\frac{i_a}{q}$ is

$$S_{i_a/q}(\omega) = 2\left(\frac{R_a}{L}S_0 + 2E_{vc}S_0\right) \quad , \tag{8.10}$$

which satisfies the fluctuation-dissipation theorem for the amplifying process and also includes the noise due to stimulated absorption. The origin of this noise current is also the dipole moment noise source. Therefore, i_a is correlated with noise current i_b. The power spectrum of the mutual correlation function is

$$S_{i_a i_b/q^2}(\omega) = -2(E_{cv}E_{vc})S_0 \quad . \tag{8.11}$$

The circuit equation for the second process (assuming $R_a \to 0$) is

$$(i\omega L + R_0)i_L = -R_0 i_0 \quad , \tag{8.12}$$

or equivalently

$$\frac{d}{dt}\Delta S = -\frac{R_0}{L}\Delta S - \frac{i_0}{q} \quad . \tag{8.13}$$

Here, relation $\frac{R_0}{L} = \gamma$ is used. The power spectral density of noise source $\frac{i_0}{q}$ is

$$S_{i_0/q}(\omega) = 2\gamma S_0 \quad , \tag{8.14}$$

which satisfies the fluctuation-dissipation theorem for the decay process. The origin of this noise current is the incident vacuum field fluctuation. Combining Eqs. (8.9) and (8.13) gives

$$\frac{d}{dt}\Delta S = -[\gamma - (E_{cv} - E_{vc})]\Delta S + \frac{1}{q}(i_a - i_0) \quad . \tag{8.15}$$

Junction voltage fluctuation υ_n and photon current fluctuation i_L are coupled via capacitance C and inductance L. The circuit equations for υ_n and i_L are

$$\upsilon_n = i\omega L i_L + (i_L + i_a)(-R_a) + (i_L + i_0)R_0 \quad , \tag{8.16}$$

and

$$i_L = -\left(\frac{1}{R_S} + \frac{1}{R} + i\omega C\right)\upsilon_n + i_s + i_b \quad . \tag{8.17}$$

The Langevin equations for the internal electron-number fluctuation and internal photon-number fluctuations are obtained by replacing $i\omega$ with $\frac{d}{dt}$ and by using relations $\upsilon_n = \frac{q}{c}\Delta N_c$ and $i_L = q\gamma\Delta S$ to give

$$\frac{d}{dt}\Delta N_c = -\left(\frac{1}{CR_S} + \frac{1}{\tau_n}\right)\Delta N - \gamma\Delta S + \frac{1}{q}(i_s + i_b) \quad , \tag{8.18}$$

$$\frac{d}{dt}\Delta S = -[\gamma - (E_{cv} - E_{vc})]\Delta S + \frac{\Delta S}{\tau_{\rm st}} + \frac{1}{q}(i_a - i_0) \quad . \tag{8.19}$$

Equation (8.18) is different from the conventional Langevin equation for the electron-number fluctuation, as can be stated with the following two points: there is a new decay rate of the electron-number fluctuation, which represents the junction-voltage pinning effect by the source, and the pump noise is not proportional to the pump rate, but is given by the thermal noise current i_s. When R_S is very large, decay rate $\frac{1}{CR_S}$ of the electron-number fluctuation becomes small, and accordingly, the pump noise becomes small.

8.1.2 Threshold for amplitude squeezing

The input electron flux fluctuation, i.e., the external circuit current fluctuation $i_{\rm in}$, is given by Kirchhoff law

$$i_{\rm in} = \frac{\upsilon_n}{R_S} + i_s \quad . \tag{8.20}$$

Junction voltage fluctuation υ_n is partly caused by noise current i_s from the (reservoir) pump sorce, as shown in Eq. (8.1). Therefore, υ_n and i_s are correlated. Junction voltage fluctuation υ_n, in turn, affects external current $i_{\rm in}$ flowing in the source resistance. This is the boundary condition at the energy input plane and represents the back action of system υ_n on the (reservoir) pump source.

The output photon flux fluctuation, i.e., the external photon current fluctuation, is given by the Kirchhoff law

$$i_{\rm out} = i_L + i_0 \quad . \tag{8.21}$$

Photon current fluctuation i_L is partly caused by noise current i_0 from the (reservoir) external photon fields (vacuum fluctuations), as shown in Eq. (8.13). Therefore, i_L and i_0 are correlated. Photon current fluctuation i_L, in turn, affects external current $i_{\rm out}$ flowing in the load resistance. This is the boundary condition at the energy output plane and represents the back action of system i_L on the (reservoir) external photon fields.

The external photon current fluctuation is related to output field fluctuation $\Delta\hat{r}$ as

$$i_{\rm out} \leftrightarrow q2r_0\Delta\hat{r} \quad , \tag{8.22}$$

and the internal photon current fluctuation is related to internal field fluctuation $\Delta\hat{A}$ as

$$i_L \leftrightarrow q\gamma 2A_0\Delta\hat{A} \quad . \tag{8.23}$$

Using relation $r_0 = \sqrt{\gamma}A_0$, boundary condition Eq. (8.21) is reduced to

$$\hat{r} = -\hat{S}_A + \sqrt{\gamma}\hat{A} \quad , \tag{8.24}$$

where $\hat{S}_A$ is an incident vacuum field.

From circuit equations Eqs. (8.16) and (8.17), v_n and i_L are obtained in a low-frequency limit as

$$v_n \simeq (R_0 - R_a)i_s + (R_0 - R_a)i_b + R_0 i_0 - R_a i_a \quad , \tag{8.25}$$

$$i_L \simeq i_s + i_b + \left(\frac{1}{R_S} + \frac{1}{R}\right) R_a i_a - \left(\frac{1}{R_S} + \frac{1}{R}\right) R_0 i_0 \quad . \tag{8.26}$$

Using the boundary conditions Eqs. (8.20) and (8.21), $i_{\rm in}$ and $i_{\rm out}$ are

$$i_{\rm in} = \left(1 + \frac{R_0 - R_a}{R_S}\right) i_s + \frac{R_0 - R_a}{R_S} i_b - \frac{R_0}{R_S} i_0 + \frac{R_a}{R_S} i_a \quad , \tag{8.27}$$

$$i_{\rm out} = i_s + i_b + \left(\frac{1}{R_S} + \frac{1}{R}\right) R_a i_a + \left[1 - \left(\frac{1}{R_S} + \frac{1}{R}\right) R_0\right] i_0 \quad . \tag{8.28}$$

Here, threshold condition $R_0 \simeq R_a$ is used. As R_S approaches infinity, $i_{\rm in} = i_s \to 0$ and

$$i_{\rm out} = \left(1 - \frac{R_0}{R}\right) i_0 + i_b + \frac{R_a}{R} i_a \simeq -x i_0 + i_b + (1+x) i_a \quad , \tag{8.29}$$

where $x = \frac{1}{n_{\rm sp}(P/P_{\rm th}-1)} = \frac{1}{n_{\rm sp}R_P}$ and $\frac{R_0}{R} \simeq \frac{R_a}{R} \simeq \frac{\tau_{\rm st}}{\tau_n} \simeq 1 + x$ are used. The power spectrum of the output photon flux is

$$S i_{{\rm out}/q}(\omega) = 2\gamma S_0 \left[2n_{\rm sp} \cdot x^2 + x\right] \quad . \tag{8.30}$$

Since $2\gamma S_0$ is the shot-noise-limited output photon flux fluctuation, Eq. (8.30) can be reduced to below the shot-noise level when pump rate $R_P \equiv P/P_{\rm th} - 1$ satisfies

$$R_P \geq \frac{4}{\sqrt{8n_{\rm sp}+1} - 1} \quad . \tag{8.31}$$

When $n_{\rm sp} = 1$ (complete population inversion), pump rate $P/P_{\rm th} \geq 3$ is required to produce a number-phase squeezed state. This "threshold pump rate" decreases with the population inversion parameter. As x approaches infinity, $i_{\rm out} \to 0$. Thus, the input electron flux and the output photon flux do not fluctuate. This is reasonable because the fixed number of electrons is injected by the high-impedance constant current source, and all the injected electrons are converted to lasing photons by the dominant stimulated emission process and are extracted from the output coupling mirror.

8.1.3 Numerical examples

Circuit elements R, $R_{\rm se} = R_0 - R_a$, L, and C in the noise equivalent circuit (Fig. 8.1) versus normalized pump level $R_P = P/P_{\rm th} - 1$ are shown in Fig. 8.2 for a typical semiconductor laser. The following numerical parameters are assumed: spontaneous emission lifetime $\tau_{\rm sp} = 3$ nsec, nonradiative electron lifetime $\tau_{\rm nr} = \infty$, stimulated emission lifetime $\tau_{\rm st} \simeq \tau_{\rm sp}/n_{\rm sp}R_P$, population inversion parameter $n_{\rm sp} = E_{cv} - E_{vc} = 2$, photon lifetime $\tau_P = 2$ psec (or the photon decay rate, $\omega/Q = 5 \times n^{11}{\rm sec}^{-1}$), stimulated emission rate $E_{cv} = n_{\rm sp}(E_{cv} - E_{vc}) \simeq n_{\rm sp}(\omega/Q) = 10^{12}{\rm sec}^{-1}$, absorption rate $E_{vc} \simeq 5 \times 10^{11}{\rm sec}^{-1}$, thermal voltage $V_T = 26{\rm mV}$, parameter $m = 1.5$, spontaneous emission coefficient $\beta = 1 \times 10^{-5}$, total photon-number $S_0 = R_P n_{\rm sp}/\beta$, active-layer volume $V = 3 \times 10^{-10}{\rm cm}^3$, and threshold electron density $N_c/V = 1.5 \times 10^{18}{\rm cm}^{-3}$.

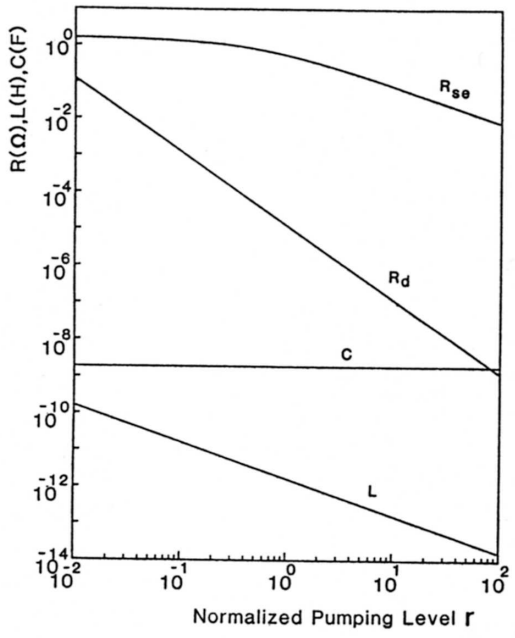

Figure 8.2: The diode's differential resistance, R, diffusion capacitance C, effective resistance $R_{\rm se}$, and effective inductance L versus normalized pump level $R_P = P/P_{\rm th} - 1$.

The power spectra for the external field amplitude fluctuation in the injection current-driven semiconductor laser with suppressed-pump fluctuation are shown in Fig. 8.3. The amplitude fluctuation spectrum for the injection current-driven semiconductor laser is reduced to below the standard quantum limit in the frequency region below the cavity bandwidth.

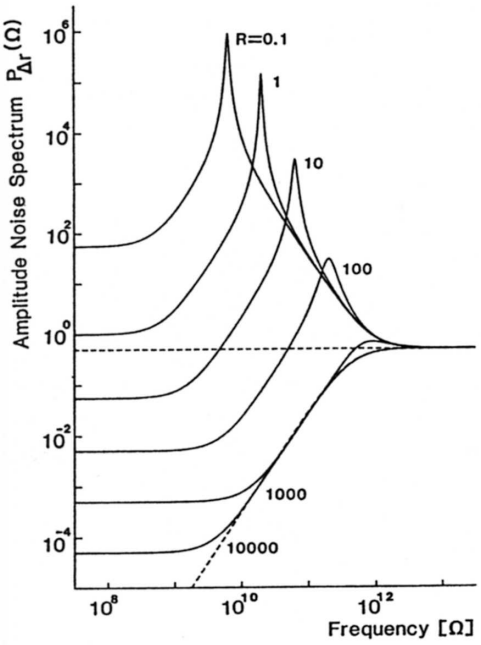

Figure 8.3: Amplitude noise spectra as a function of a normalized pump level R_P; with suppressed pump noise.

The amplitude fluctuation power spectral densities in the low-frequency region are shown in Fig. 8.4 as a function of series resistance R_S. Since diode differential resistance R decreases monotonically with the pump level, as shown in Fig. 8.2, criterion $2R < R_S$, wherein the pump fluctuation becomes smaller than the shot-noise level, is always satisfied for any finite R_S value. Figures 8.4(a) and 8.4(b) correspond to the respective cases of no internal loss ($\omega/Q_0 = 0$ and $\omega/Q_e = \omega/Q = 5 \times 10^{11}\text{sec}^{-1}$) and finite internal loss ($\omega/Q_0 = 1 \times 10^{11}\text{sec}^{-1}$ and $\omega/Q_e = 4 \times 10^{11}\text{sec}^{-1}$). The amplitude squeezing is reduced by the presence of cavity internal loss.

8.1.4 Experimental results

A. Observation of amplitude squeezing by balanced detectors with a delay line

In a usual intensity noise measurement, two measurement steps are required; one for a laser intensity noise measurement and the other for a shot noise calibration with a light emitting diode. To eliminate the error introduced by the two-step measurements and the

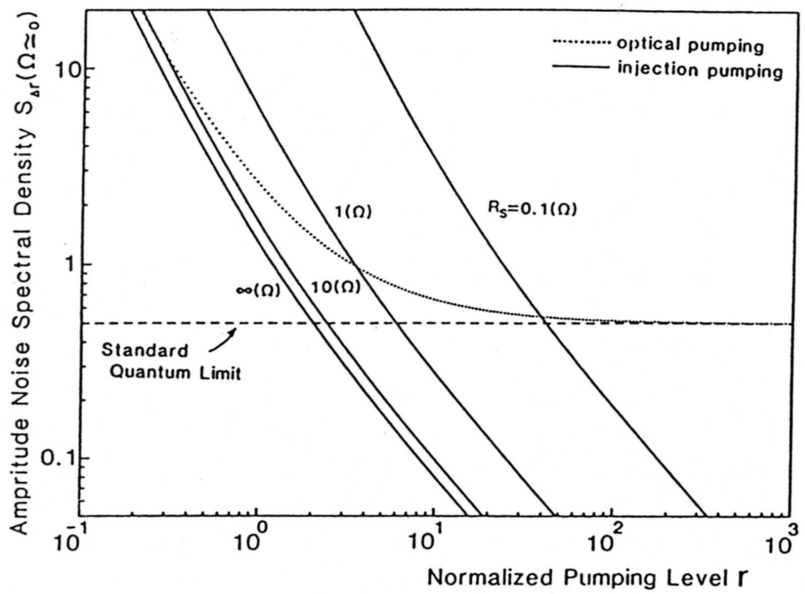

(a)

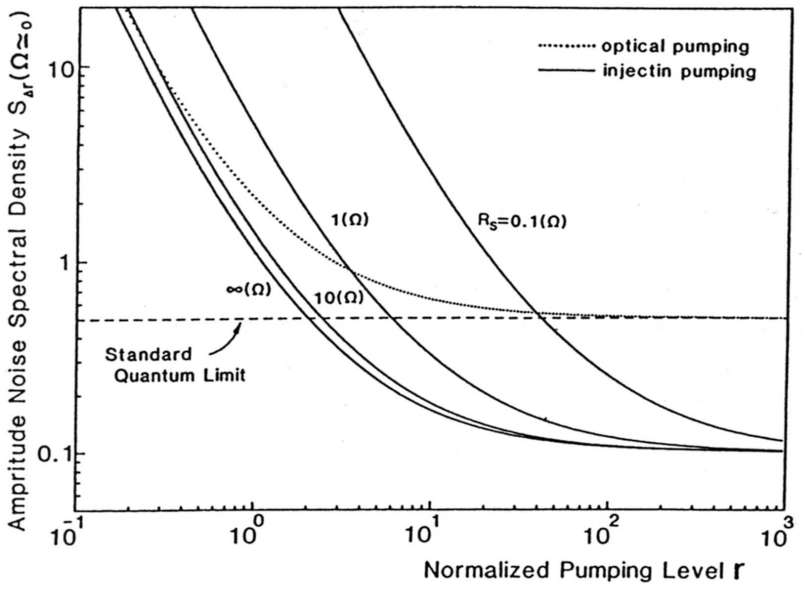

(b)

Figure 8.4: Amplitude noise spectral densities in the low-frequency region, $\Omega \ll \omega/Q$ versus normalized pump level R_P. The dotted line and solid line correspond to the optical pumping with shot-noise-limited pump amplitude fluctuation and the injection pumping with a source resistance R_S; (a) with no internal loss $\omega/Q_0 = 0$; (b) with a finite internal loss $\omega/Q_0 = 1 \times 10^{11}\mathrm{s}^{-1}$.

photodetector saturation effect dependent on a beam spot size, the balanced detectors with a delay line shown in Fig. 8.5 are developed[6]. One detector output is delayed (by $\tau = 50$ nsec in our measurement), but the other detector output is not. The difference in these two outputs is produced by a differential amplifier. A coaxial cable delay line has a loss coefficient proportional to $\sqrt{\Omega}$, where Ω is the fluctuation frequency. This frequency-dependent attenuation imposed on the delayed signal is compensated for by introducing the same attenuation to the other signal.

For a fluctuation frequency $\Omega_{\rm in}$ satisfying inphase delay condition $\Omega_{\rm in}\tau = 2N\pi$, where N is an integer, the differential amplifier output measures $\hat{I}_1 - \hat{I}_2$, where $\hat{I}_1$ and $\hat{I}_2$ are the two photodetector currents. The current-fluctuation spectral density is exactly equal to the shot-noise level. For a fluctuation frequency $\Omega_{\rm out}$ satisfying out-of-phase delay condition $\Omega_{\rm out}\tau = (2N+1)\pi$, the differential amplifier output measures $\hat{I}_1 + \hat{I}_2$. The quantum-mechanical theory of a balanced detector[7] shows that $\hat{I}_1 + \hat{I}_2$ measures the quantum noise of the laser itself. Thus, the detector output simultaneously displays the laser-noise level and the corresponding shot-noise level on a spectrum analyzer with a frequency period of $\Delta\Omega = 2\pi/\tau$.

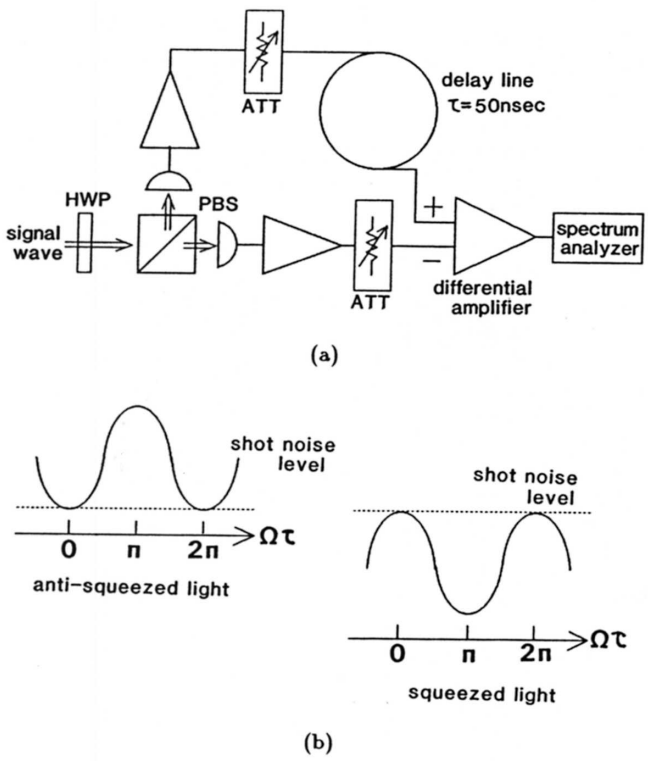

Figure 8.5: (a) Balanced direct detectors with a delay line and attenuators (ATT). (b) Current noise spectra of an amplitude antisqueezed light and an amplitude-squeezed light.

When the signal wave is amplitude-anti squeezed (super-Poissonian), the current fluc-

tuation at $\Omega_{\rm in}$ is smaller than that at $\Omega_{\rm out}$, as shown in Fig. 8.5(b). On the other hand, when the signal wave is amplitude squeezed (sub-Poissonian), the current fluctuation at $\Omega_{\rm in}$ is larger than that at $\Omega_{\rm out}$, as shown in Fig. 8.5(b). This inverted modulation in the current-fluctuation spectrum is an unmistakable mark of amplitude-squeezed light. This is a single-step measurement; therefore, the ambiguity in the shot-noise level owing to the photodetector saturation can be eliminated.

Figure 8.6 shows current noise spectra at two different bias levels. The current noise spectrum for bias level $R_P = 0.03$, which is shown by curve A, features lower noise power at $\Omega_{\rm in}$ than at $\Omega_{\rm out}$. This indicates that the field is amplitude antisqueezed (super-Poissonian). The amplifier noise level is shown by curve B. The current noise spectrum for bias level $R_P = 12.6$, which is shown by curve C, features higher noise power at $\Omega_{\rm in}$ than at $\Omega_{\rm out}$. This indicates that the field is amplitude squeezed (sub-Poissonian). The total dc photocurrents are 15μA and 6.12 mA for $R_P = 0.03$ and 12.6, respectively. Curves D and E are the current noise spectra when one of the two incident signal waves for $R_P = 12.6$ is blocked. The modulation disappears, as expected, in a low-frequency region. At high frequencies, however, the noise power is reflected back at the differential amplifier input, and so the modulation due to the round trip in a delay line appears. Curve F is the sum of the current noise spectra indicated by curves D and E. The noise level of curve F is not equal to a 3 -dB noise rise form the noise level indicated by curves D or E because of the amplifier thermal noise (curve B). Note that the current noise spectrum indicated by curve F is between the shot-noise level at $\Omega_{\rm in}$ and the reduced noise level at $\Omega_{\rm out}$. This is because of the noise level of amplitude-squeezed light increases to approach the shot-noise level when the amplitude is attenuated.

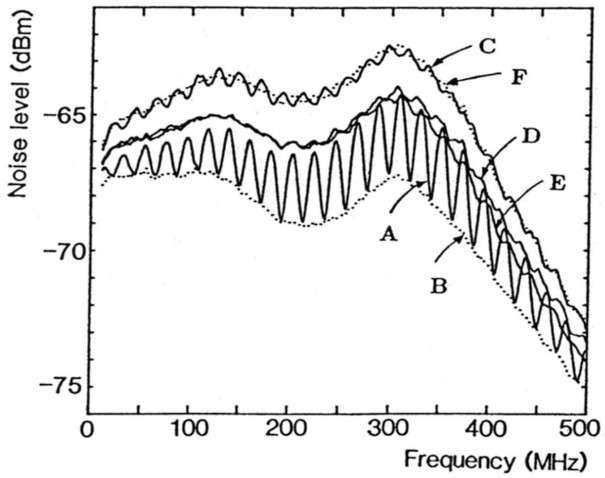

Figure 8.6: Current noise spectra for bias levels $I/I_{\rm th} = 1.03$ (curve A) and $I/I_{\rm th} = 13.6$ (curve C). Curve B is the amplifier thermal noise. Curves D and E are obtained when one of the two signal beams is blocked for $I/I_{\rm th} = 13.6$. Curve F is the sum of noise curves D and E.

Figure 8.7 shows the current noise spectra normalized by the shot-noise level for the two bias levels. The shot-noise level calibrated by the measurement of $\hat{I}_1 - \hat{I}_2$ is compared with the shot-noise level generated by the light-emitting diode with the same wavelength as the laser. The difference is smaller than 0.1 dB. The current noise spectrum at $R_P = 0.03$ shows an enhanced noise peak at the relaxation-oscillation frequency. The current noise spectrum at $R_P = 12.6$ shows a noise level reduced to -1.3 dB below the shot-noise level. The observed 0.6-dB squeezing becomes 1.3-dB squeezing in Fig. 8.7, because the effect of the amplifier thermal noise is subtracted. This noise reduction is much larger than the error bar of the shot-noise-level calibration.

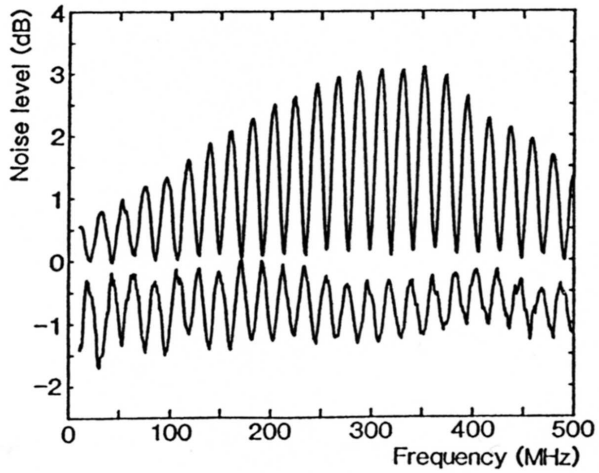

Figure 8.7: Current noise spectra normalized by the shot-noise level for bias levels $I/I_{\rm th} = 1.03$ (upper curve) and $I/I_{\rm th} = 13.6$ (lower curve). The amplifier thermal noise is subtracted in the normalization process.

B. Amplitude squeezing vs. pump rate

The degree of squeezing is degraded by the Poissonian partition noise associated with optical loss. To increase the light collection efficiency, a GaAs transverse junction stripe laser, with less than 3% front facet reflectivity R_1 and more than 90% rear facet reflectivity R_2, is operated at 66 K to minimize the free carrier absorption loss and is directly coupled to photodetector to minimize the coupling loss. Figure 8.8 shows theoretical and experimental photon number noise values normalized by the shot noise value versus the normalized pump rate $I/I_{\rm th} - 1$[8]. The experimental results are corrected for a detection quantum efficiency of about 89%, so the degree of squeezing shown in Fig. 8.8 corresponds to that of the laser output. The experimental maximum degree of squeezing, -14 dB ($\simeq 0.04$), is in

reasonable agreement with the theoretical limit imposed by the output coupling efficiency

$$\eta = \frac{\ln\left(\frac{1}{R_1}\right)}{\ln\left(\frac{1}{R_1 R_2}\right)} \simeq 0.97$$

of the laser.

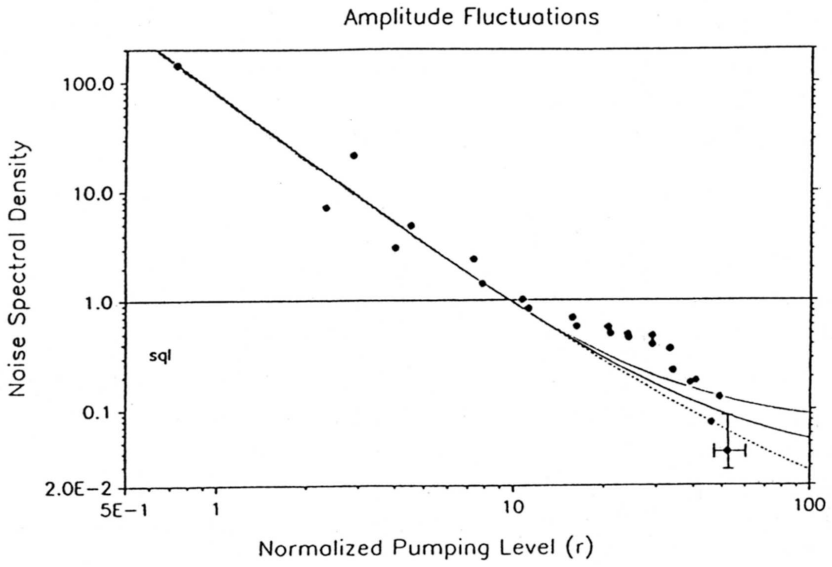

Figure 8.8: The theoretical (lines) and experimental (•) intensity noise values normalized by the shot noise value versus the normalized rate $R \equiv I/I_{\rm th} - 1$. The experimental results are corrected for a detection quantum efficiency of 89%.

8.2 Excess Noise in Avalanche Photodiode

8.2.1 Conventional (Markov) process in the avalanche process

In this section, we review the conventional avalanche photodiode (APD), the theory of which is well developed[9]. Photoelectrons are introduced into high-field regions where an avalanche of secondary, tertiary, $\cdots$ electrons is generated by successive impact ionization. However, in a typical APD, photoionization and impact ionization each promote electrons from the valence band; in the SSPM, photoionization and impact ionization each promote electrons from neutral impurities. One consequence is that the fields typically employed in an APD to achieve impact ionization are at least 50 times those employed in the SSPM. This difference will turn out to be significant to the development of a model for the pulse-amplitude distribution of the SSPM. Another consequence is that in the APD, both electrons and holes may generate carriers by impact ionization, whereas only electrons

generate carriers in the SSPM. However, the best performance in an APD is obtained when only one type of carrier undergoes multiplication; in this sense, the SSPM is an ideal APD. For purposes of comparison, hereafter we consider only an ideal APD, i.e., with one type of avalanching carrier. Finally, a typical APD (operating with electric fields below breakdown) generates an electron pulse in response to a group of between 50 and 250 photoelectrons.

In the usual treatments of the APD, the calculation of the pulse-amplitude distribution $h(n)$ employs a phenomenological rate α which is the probability per unit length that a carrier generates another carrier via impact ionization[9]. Usually α is described as varying, at most, with the instantaneous position r of a carrier with respect to the field axis. Since α is independent of the history of carrier in APDs, the avalanche develops as a Markov process. If, in addition, the carriers do not interact with each other, the avalanche may be described by the classical theory of branching. Since we consider only an ideal APD, the theory amounts to a one-dimensional Markov branching process for one type of carrier undergoing multiplication. With the restrictions just discussed, the branching theory yields $p(n, r; m)$, i.e., the probability that there are n electrons at r, given exactly m electrons injected into the avalanche region. In what follows, the origin of the high-field region is set to $r = 0$, and terminates at $r = L$. The pulse-amplitude distribution is then $h(n) \equiv p(n, L; m)$. Since the SSPM is a photon counter, we ask the theory to find $h(n)$ for $m = 1$.

Then, for any continuous $\alpha(r)$, $p(n, r; m)$ must satisfy the following rate equations:

$$\begin{aligned} \frac{\partial p(m,r;m)}{\partial r} &= -m\alpha(r)p(m,r;m) \quad , \\ \frac{\partial p(n,r;m)}{\partial r} &= -n\alpha(r)p(n,r;m) \\ &\quad +(n-1)\alpha(r)p(n-1,r;m) \; , \quad n > m \quad , \end{aligned} \tag{8.32}$$

with the initial conditions $p(m, 0; m) = 1$, $p(n, 0; m) = 0$, and $m \geq 1$. The solution is

$$p(n,r;m) = \left(\begin{array}{c} n-1 \\ n-m \end{array} \right) [Z(r)-1]^{-m} \left(1 - \frac{1}{Z(r)}\right)^n \quad , \tag{8.33}$$

where

$$Z(r) = \exp\left(\int_0^r ds\alpha(s)\right) \quad .$$

These probabilities obey the normalization $\sum_{n=1} p(n, r; m) = 1$. The mean pulse amplitude as a function of position is $\langle n(r)\rangle = mZ(r)$. In the single-photon counting mode, $m = 1$; the resulting distribution for any $\alpha(r)$ is

$$h(n) \equiv p(n, L; 1) = (1 - 1/\langle n\rangle)^n/(\langle n\rangle - 1) \quad , \tag{8.34}$$

which is a monotonically decaying function with $\langle n\rangle = Z(L)$, far from its peak at $n = 1$. For $\langle n\rangle \gg 1, h(n) \simeq \exp(-n/\langle n\rangle)/\langle n\rangle$.

Ignoring the fluctuations in this number as well as in their initial position, the pulse-amplitude distribution is described by $p(n, L; m)$ above, which for sufficiently large m is

a unimodal function peaked near the mean pulse amplitude. Figure 8.9 illustrates this difference with a comparison between $p(n, L; m)$ and $p(n, L; 1)$ for an ideal APD with $L = 10\mu$m. The model APD responds in the first case to exactly $m = 11$ photoelectrons with a gain (defined here as $\langle n \rangle / m$) of 100 ($\alpha = 0.4605\ \mu\text{m}^{-1}$) and in the other to exactly $m = 1$ photoelectron with a gain of 1100 ($\alpha = 0.7003\mu\text{m}^{-1}$), so that in both cases the mean pulse amplitude is 1100 electrons. We will return to this example in the next section.

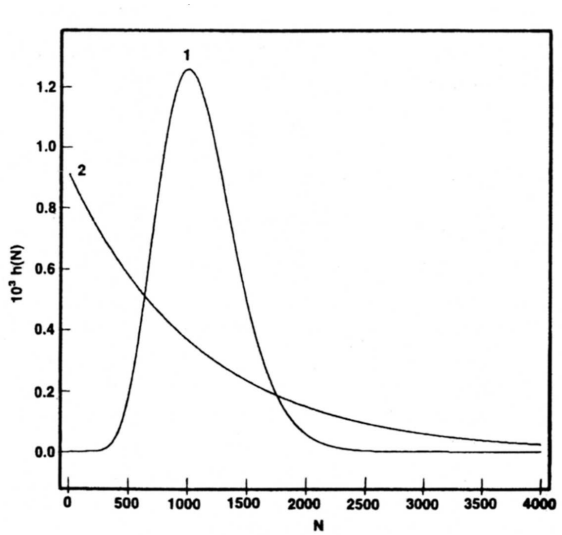

Figure 8.9: The pulse-amplitude distribution $h(n)$ for the model APD calculated from Eqs. (8.33) and (8.34). Curve 1 shows $h(n) = p(n, L; 11)$ for the APD when it generates an avalanche in response to exactly 11 photoelectrons, with a gain of 100. Curve 2 shows $h(n) = p(n, L; 1)$ for the APD when it responds to exactly one photoelectron, with a gain of 1100. The mean pulse amplitude ($\langle n \rangle = 1100$) is the same for both curves.

As we show in the following section, the Markov (i.e., history-independent) property of the branching process provides an essentially correct description of the APD, mainly because the electric fields are so high that they accelerate the newly born electrons almost instantly to the energies required for their subsequent impact ionization. On the contrary, the electric fields encountered by the electrons in the SSPM are so low that they must traverse considerable distances before they attain energies sufficient for impact ionization. The demonstration of this history dependence can be made explicit with a standard Monte-Carlo simulation for a single electron in the high-field region of the SSPM, with which we begin the next section.

8.2.2 A non-Markov process in low-field avalanche photodiodes

By rejecting the Markov hypothesis implied by Eqs. (8.32)-(8.34), we assume that the branching process depends on the history of the electron. In this section we calculate by

standard Monte Carlo techniques the distance traveled by a single electron between its birth and its first attainment to the energy required for impact ionization. We conclude this section with the application of the results to the non-Markovian extension of Eqs. (8.32)-(8.34).

The Monte Carlo calculation for single-electron transport (which solves the semi-classical Boltzmann equation) in semiconductor devices has been extensively reviewed elsewhere[10]; we confine ourselves to a listing of some of the parameters involved. For the SSPM, we limit the (three-dimensional) electron transport to a 4-μm-thick high-field region where, for simplicity and for comparison to the APD, a constant field is applied along the field axis. The fields E employed are assigned strengths of 3, 3.5, and 4 kV/cm, respectively. In addition to the usual formulas for the acoustic intervalley and acoustic-optic intravalley phonon scattering rates (which reproduce experimental electron transport data)[10], we employ Erginsoy's formula for the neutral impurity scattering[10]. The low compensation (set to zero) and the low temperature (set to 10 K) encountered in the SSPM suggest a lack of significant ionized impurity scattering, and is therefore omitted in this calculation. The ionization energy of arsenic donors in cryogenic silicon with low compensation is taken to be 54 meV; their density N_d is set to $5 \times 10^{17}\text{cm}^{-3}$ throughout the infrared-active layer.

The calculation proceeds as follows. One photoelectron is introduced into the high-field region with a random velocity corresponding to a kinetic energy of 1 meV. As the electron is accelerated toward the blocking layer by the field, phonon and impurity scattering delay its attainment of the ionization threshold. When ionization energy is finally attained, its position projected onto the field axis is recorded. Since the energy of the interrupted electron always exceeds the ionization energy, we make the approximation that impact ionization occurs instantaneously. Therefore, the energy remaining to the two new electrons (after the ionization energy is subtracted) is randomly partitioned and the trajectory for the randomly chosen electron resumes with a randomized velocity corresponding to its share of the energy. The electron continues to be accelerated by the field until once again threshold is first exceeded. This interrupted trajectory continues until the blocking layer is reached. Five hundred trajectories were run in this fashion, and the distance x between an electron's birth and its attainment of threshold were scored in a normalized histogram $f(x)$. Since the field is constant, we regard the threshold distance distribution $f(x)$ as independent of position.

The first moment of $f(x)$ yields the mean distance $\bar{x}$ traveled between birth and threshold, namely, $\bar{x} \approx 0.22\mu$m (for $E = 3$ kV/cm), roughly 6% of the distance of the entire high-field region in which the avalanche develops. For comparison, we also consider a calculation appropriate for electrons in an ideal silicon APD which in this case responds to exactly one photoelectron. For this model APD, operating at 300 K, we consider an undoped high-field region 10 μm thick, with an applied constant field of 400 kV/cm. The resulting threshold distance distribution $f(x)$ (determined from 500 trajectories) has $\bar{x} \approx 0.047\mu$m, about $\frac{1}{2}$% of the entire avalanche region in an APD, and about one-fifth the mean distance found for the model SSPM. Figure 8.10 shows $f(x)$ for the model SSPM (for $E = 3$ kV/cm) and the model APD, respectively. By comparison with the SSPM, the $f(x)$ for the APD is approximately a delta function at the origin, and therefore the assumption of history independence for the avalanching carriers is apparently an excellent one. The substantially displaced and more disperse threshold distribution exhibited by

the SSPM, however, suggests that the history dependence of the electrons may be important. In order to pursue this suggestion, we now display the non-Markovian extension of Eqs. (8.32)-(8.34) for $h(n)$.

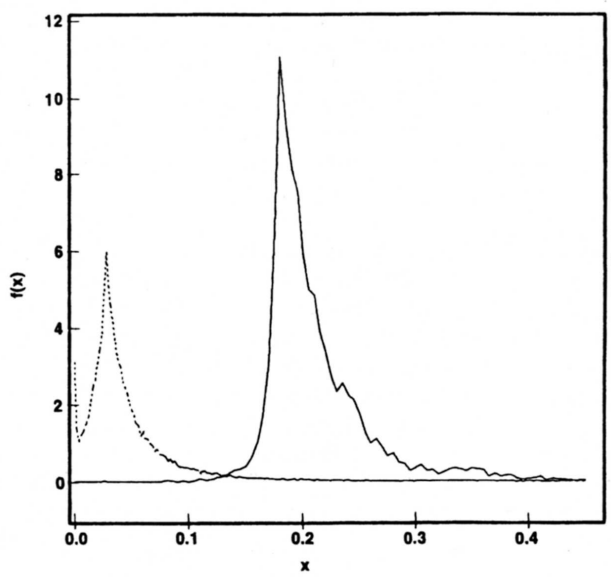

Figure 8.10: The threshold-distance distribution $f(x)$ calculated from 500 one-electron Monte Carlo trajectories. The solid curve shows $f(x)$ for the model SSPM,($E = 3$ kV/cm). The dashed curve shows $f(x)$ for the model APD ($E = 400$ kV/cm).

The non-Markov branching equations, like the Markov equations of Eq. (8.32), have for input a phenomenological branching rate α, which the additional dependence of α on the "age" (i.e., the distance traveled between birth and threshold) x of the electron. Although, as in the Markov case, α may also depend on the position r, the applied electric field in the models considered is constant, and therefore we only consider a position-independent, age-dependent rate $\alpha(x)$. The rate $\alpha(x)$ is related to the foregoing threshold distance distribution $f(x)$ by

$$\alpha(x) = k \int_0^x ds f(s) \quad , \tag{8.35}$$

where k is a phenomenological rate constant (with units of μm^{-1}), and $\int_0^x ds f(s)$ is the cumulative probability that an electron has reached threshold. Figure 8.11 shows the cumulative threshold distributions obtained by numerical integration[11] for both the model SSPM (for $E = 3$ kV/cm) and the model APD (for $E = 400$ kV/cm). With these definitions, the probability $p(n, r; 1)$ that there are n electrons at r given exactly one photoelectron at the origin of the high-field region is supplied by

$$\frac{\partial p(1, x; 1)}{\partial x} = -\alpha(x) p(1, x; 1) \equiv \psi(x) \quad ,$$

$$p(n,r;1) = -\int_0^r dx\psi(r-x)\sum_{m=1}^{n-1} p(m,x;1)p(n-m,x;1) \quad ,$$
$$n > 1 \quad , \tag{8.36}$$

with the initial conditions $p(0,r;1)=0$ and $p(1,0;1)=1$. The Markovian equations (with a position independent α) for $p(n,r;1)$ are recovered when $\alpha(x)=k$, i.e., when

$$\int_0^x dsf(x) = 1$$

for all x. As Fig. 8.11 shows, the rate is essentially history independent for the model APD, whereas for the model SSPM, there is a small but significant deviation from Markovian behavior.

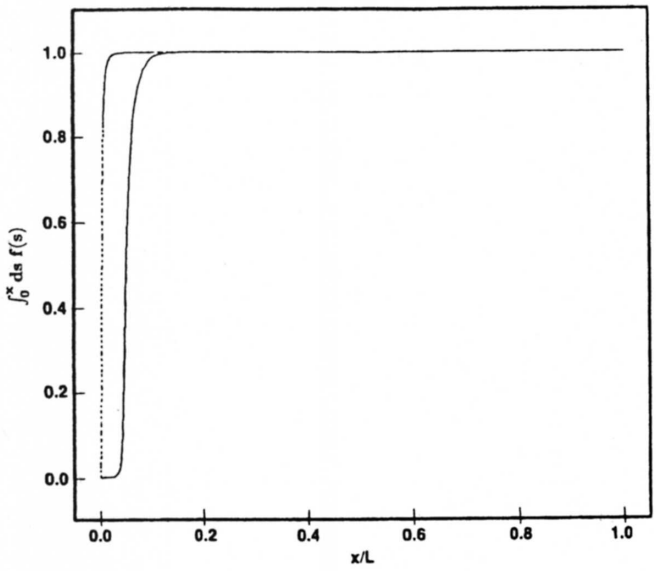

Figure 8.11: The cumulative threshold-distance distribution $\int_0^x dsf(s)$, vs. x/L. The solid curve corresponds to the model SSPM, $L = 4\mu$m. The dashed curve corresponds to the model APD, $L = 10\mu$m. The Markovian case corresponds to $\int_0^x dsf(s) = 1$ for all x.

Equations (8.35) and (8.36) constitute the non-Markovian extension of the branching theory of Eqs. (8.22) and (8.23). In the following we discuss the solution to Eq. (8.36) for both the model SSPM and the model APD.

The corresponding numerical solution of Eq. (8.36) for the model SSPM is complicated by the large number of electrons generated in the avalanche, which exceeds the limits on available computer memory. Fortunately, as the results will show, the first four moments are sufficient to accurately describe the probabilities $p(n,r;1)$ for the model SSPM. The first four moments of $p(n,r;1)$ are defined by

$$\langle n^j(r)\rangle \equiv \sum_{n=1} n^j p(n,r;1) \tag{8.37}$$

for $j = 1 \ldots 4$, respectively. Combining Eqs. (8.36) and (8.37) yields the hierarchy of integral equations for the moments:

$$\begin{aligned}
\langle n(r)\rangle &= p(1,r;1) - 2\int_0^r dx\psi(r-x)\langle n(x)\rangle \quad , \\
\langle n^2(r)\rangle &= p(1,r;1) - 2\int_0^r dx\psi(r-x) \\
&\quad \times\Big[\langle n^2(x)\rangle + \langle n(x)\rangle^2\Big] \quad , \\
\langle n^3(r)\rangle &= p(1,r;1) - 2\int_0^r dx\psi(r-x) \\
&\quad \times\Big[\langle n^3(x)\rangle + 3\langle n^2(x)\rangle\langle n(x)\rangle\Big] \quad , \\
\langle n^4(r)\rangle &= p(1,r;1) - 2\int_0^r dx\psi(r-x) \\
&\quad \times\Big[\langle n^4(x)\rangle + 3\langle n^2(x)\rangle^2 4\langle n^3(x)\rangle\langle n(x)\rangle\Big] \quad .
\end{aligned}$$

Various methods exist for the approximate reconstruction of the probabilities $p(n,r;1)$ from a fixed number of their moments. For the SSPM, Edgeworth's method[12] is sufficiently accurate, and with $\langle n^j\rangle \equiv \langle n^j(L)\rangle$, provides

$$\begin{aligned}
h(n^*) \approx\ & \eta(n^*)\left(1 + \frac{\gamma}{6}(n^{*3} - 3n^*) + \frac{\kappa}{24}(n^{*4} - 6n^{*2} + 3)\right. \\
& \left. + \frac{\gamma^2}{72}(n^{*6} - 15n^{*4} + 45n^{*2} - 15)\right) \quad , \qquad (8.38)
\end{aligned}$$

where

$$\begin{aligned}
n^* &\equiv (n - \langle n\rangle)/\sigma \quad , \\
\sigma^2 &\equiv \langle (n - \langle n\rangle)^2\rangle \quad , \\
\gamma &\equiv \langle (n - \langle n\rangle)^3\rangle/\sigma^3 \quad , \\
\kappa &\equiv \langle (n - \langle n\rangle)^4\rangle/\sigma^4 - 3 \quad ,
\end{aligned}$$

and

$$\eta(x) \equiv (1/\sqrt{2\pi})\exp(-x^2/2) \quad .$$

The Edgeworth formula describes a Gaussian distribution perturbed by a finite skew γ and kuritosis κ, respectively, and is expected to be accurate for small γ and κ.

Equations (8.37) and (8.38) are solved by standard numerical techniques, and determine $h(n)$ once $\alpha(x)$ is chosen. The $f(x)$ calculated in the last section for each of the applied fields ($E = 3, 3.5, 4$, respectively) were used to determine α for the SSPM. For each of the three fields employed in the model SSPM, we adjusted κ so that $\langle n\rangle \approx 35000$. The values for γ and κ are sufficiently low for the validity of Eq. (8.38), and also suggest the sufficiency of four moments to describe $h(n)$.

The $h(n)$ determined by Eq. (8.38) is shown in Fig. 8.12, along with the corresponding Markov prediction for the same mean pulse amplitude.

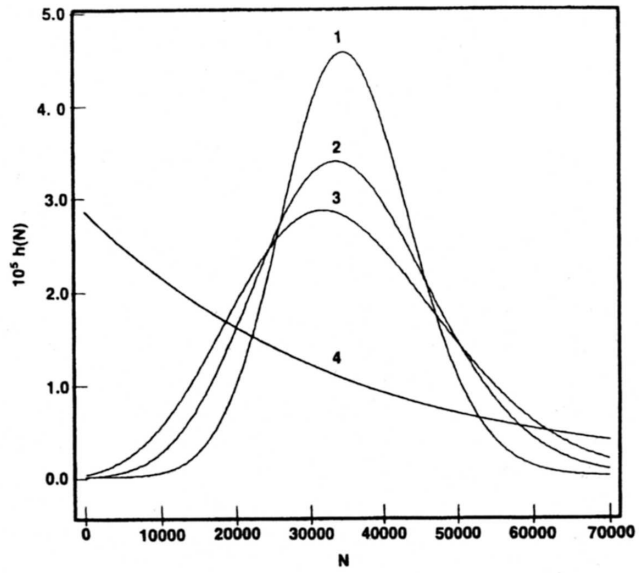

Figure 8.12: The calculated pulse-amplitude distribution $h(n)$ for the model SSPM. Curves 1, 2, and 3 show $h(n)$ for $E = 3.3.5$, and 4 kV/cm, respectively, calculated from Eq. (8.38). Curve 4 shows the Markov prediction from Eq. (8.33) with $\langle n \rangle = 35000$.

8.2.3 Discussion

Figure 8.12 shows that for the SSPM, the inclusion of non- Markovian effects in α radically alters the shape of $h(n)$; furthermore, the calculated non–Markovian $h(n)$ strongly resembles the pulse-amplitude distribution typically observed in the SSPM. Therefore, non-Markovian effects play a decisive role in the development of the electron avalanche in the SSPM, in contrast to the APD.

Figure 8.11 shows that the α for the model SSPM is essentially constant over nearly 90% of the entire high-field region. Nevertheless, the seemingly small interval of deviation from the Markovian rate is enough to produce a pulse-amplitude distribution strikingly different from the Markovian prediction. On the scale shown in Fig. 8.11, the differences between $\int_0^x dsf(s)$ which correspond to the various fields employed in the model SSPM are barely perceptible, yet the differences are readily apparent in the pulse-amplitude distributions shown in Fig. 8.12. The remarkable sensitivity of the model SSPM to the extent of non-Markovian effects, and in turn its sensitivity to small changes in the electric field, has important consequences for SSPM design.

8.2.4 Multiphoton detection using visible light photon counter

Please see the attached publication "Multiphoton detection using visible light photon counter", J. Kim et al., APL 74, 902 (1999).

Bibliography

[1] Y. Yamamoto, S. Machida and O. Nilsson, *Phys. Rev. A* **34**, 4025 (1986).

[2] S. Machida, Y. Yamamoto, and Y. Itaya, *Phys. Rev. A* **58**, 1000 (1987).

[3] J. Kim, Y. Yamamoto and H. Hogue, *Appl. Phys. Lett.* **70**, 2852 (1997).

[4] J. Kim, S. Takeuchi, Y. Yamamoto, and H. Hogue, *Appl. Phys. Lett.* **74**, 902 (1999).

[5] Y. Yamamoto, *Coherence, Amplification and Quantum Effects in Semiconductor Lasers* (Wiley, New York, 1991) p.461.

[6] S. Machida and Y. Yamamoto, *Opt. Lett.* **14**, 1045 (1989).

[7] H. P. Yuen and V. W. S. Chan, *Opt. Lett.* **8**, 177 (1983).

[8] W. H. Richardson, S. Machida, and Y. Yamamoto, *Phys. Rev. Lett.* **66**, 2867 (1991).

[9] G. E. Stillman and C. M. Wolfe, in *Semiconductors and Semimetals*, ed. by R. K. Willardson and A. C. Beer, vol. 12 (Academic, New York, 1977) p. 72.

[10] C. Jacoboni and L. Reggiani, *Rev. Mod. Phys.* **55**, 645 (1983).

[11] R. A. LaViolette and M. G. Stapelbroek, *J. Appl. Phys.* **65**, 830 (1989).

[12] H. Cramer, *Mathematical Methods of Statistics* (Princeton, New Jersey, 1946) p. 227.

Multiphoton detection using visible light photon counter

Jungsang Kim,[a] Shigeki Takeuchi,[b] and Yoshihisa Yamamoto[c]
ERATO Quantum Fluctuation Project, E. L. Ginzton Laboratory, Stanford University, Stanford, California 94305

Henry H. Hogue
Research and Technology Center, Boeing North American, Anaheim, California 92803

(Received 14 September 1998; accepted for publication 8 December 1998)

Visible light photon counters feature noise-free avalanche multiplication and narrow pulse height distribution for single photon detection events. Such a well-defined pulse height distribution for a single photon detection event, combined with the fact that the avalanche multiplication is confined to a small area of the whole detector, opens up the possibility for the simultaneous detection of two photons. In this letter, we investigated this capability using twin photons generated by parametric down conversion, and present a high quantum efficiency ($\sim$47%) detection of two photons with good time resolution ($\sim$2 ns), which can be distinguished from a single-photon incidence with a small bit-error rate ($\sim$0.63%). © *1999 American Institute of Physics.* [S0003-6951(99)00307-1]

Experimental techniques for single photon detection have made tremendous progress in recent years. High quantum efficiency and low dark counts (background noise) are considered to be the figure-of-merit in characterizing the performance of a single photon detector. Photomultiplier tubes (PMTs) and Si avalanche photodiodes (APDs)[1] have been most widely used, while alternate technologies like solid state photomultipliers (SSPMs),[2] visible light photon counters (VLPCs),[3] and superconducting tunnel junctions (STJs)[4] have recently demonstrated unique capabilities that PMTs and APDs cannot offer. The quantum efficiency required for detection efficiency loophole free test of Bell inequality (83%) has been realized by the VLPCs ($\sim$88%).[5] STJs offer single photon detection capability with some wavelength resolution ($\sim$45 nm).[4] In this letter, we report the capability of VLPCs of detecting two photons. Such capability can be used for the test of Bell inequality,[6] quantum teleportation experiments[7] and also for the enhancement of the security in quantum cryptography systems.[8]

Single photon counters should have internal gain mechanism to overcome huge thermal noise generated in the electronic circuits that follow. The noise in this multiplication process determines the distribution of pulse height generated by the single photon detection events.[9] For the detectors with low multiplication noise, the pulse height originating from a single photon detection event is well defined and there is a possibility to distinguish a single photon detection event from a two photon detection event. PMTs have low noise in the multiplication process,[10] but the single photon quantum efficiency is limited to about $<25\%$ and so the maximum two photon detection efficiency should be only 6%. High quantum efficiency can be achieved by APDs ($\sim$76%),[11] but the large multiplication noise in these devices completely washes out the correlation between the number of photons incident and the generated pulse height.[12,13] In addition to that, for the APDs that operate in Geiger mode for single photon counting, the entire diode breaks down upon detection of a single photon incidence. Therefore, it is impossible to distinguish a two-photon detection event from a single photon detection event.

VLPCs feature noise-free avalanche multiplication and the pulse height resulting from a single photon detection event is very well defined.[9,14] Furthermore, the avalanche breakdown is confined to a small portion ($\sim 20\,\mu$m diameter) of the total area (1 mm diameter) of the detector. This means that the remainder of the device is still active for another photon detection even if a single photon is detected. These properties open up a possibility for multiple-photon detection using VLPCs. Such behavior has already been observed in previous experiments where the time resolution of the electronic circuit was poor,[3] so that more than two photons are detected by the VLPC as a single pulse. In these experiments, however, a difference in the arrival time of the two photons are reflected in the pulse height, which result in significant broadening of the pulse height distribution. Exact quantum efficiency of the two photon detection and the bit-error rate for two photon detection event cannot be determined quantitatively from these experiments.

We have used twin photons generated by a degenerate parametric down-conversion process, where the delay in the arrival times of the two photons can be controlled precisely by optical path length difference.

Figure 1 shows the experimental setup. We used 351.1 nm ultraviolet (UV) radiation from an Ar^+ laser to pump a BBO crystal in type-II phase-matching configuration. The crystal was slightly tilted away from the colinear phase-matching condition, so that the signal and idler beams (both at 702.2 nm) are completely separated in space.[15] Each of the beams was collimated using a weak focusing lens. One of the beams was delayed, and the two beams were recombined using a polarizing beam splitter. The recombined beam was focused onto the surface of the VLPC through a narrow bandpass filter [centered at 702 nm, and bandwidth of 0.26

[a]Electronic mail: jungsang@loki.stanford.edu
[b]JST-PRESTO ''Field and Reactions'', A. T. R. C., Mitsubishi Electric Corporation, Amagasaki, Hyogo 661-8661, Japan.
[c]Also affiliated with NTT Basic Research Laboratories, Atsugi, Kanagawa, Japan.

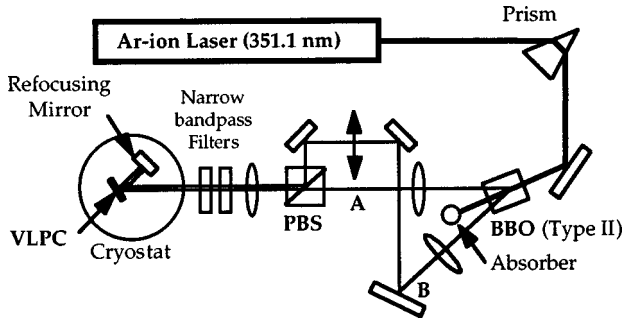

FIG. 1. A schematic of the experimental setup.

nm full-width at half-maximum (FWHM)]. We have installed the VLPC in a bath-type He cryostat where the temperature is stabilized to within 0.005 K using active temperature control. Since the VLPC is extremely sensitive to infrared photons, extensive radiation shields with acrylic windows were used to prevent the room temperature thermal radiation from reaching the detector while keeping transparency at ~97% for 702 nm photons by antireflection coating.[5] The reflected light from the surface of the detector (~16%) was recollected using a spherical refocusing mirror and the net reflection loss was reduced to ~2.5%. The output signal was amplified by a room temperature preamplifier (MITEQ AUX1347) which has a bandwidth of 500 MHz and provides electrical pulses of 2 ns in width when a single photon is detected.

Figure 2(a) shows an electrical pulse resulting from a single photon detection event. The width of the pulse (2 ns) does not decrease even when the bandwidth of the amplifier is increased, indicating that it is limited by the capacitance of the VLPC (~14 pF) and the input impedance of the amplifier (50 Ω). Figures 2(b) and 2(c) show the cases when the optical delay between the two beams is 5 and 3 ns, respectively. The heights of the pulses are almost identical, indicating that the number of electrons released per single photon detection event is well defined. Finally, Fig. 2(d) shows when the optical delay is reduced to zero. The two pulses resulting from the two photon detection events completely overlap in time, and the pulse height is twice that of a single photon detection event.

Pulse height analysis can be performed to estimate the bit-error rate for the two-photon detection event. Figure 3 shows the pulse height analysis of the cases when only one of the beams is incident [Fig. 3(a)], and when both beams are incident on the VLPC [Fig. 3(b)]. For the two-beam incidence case, there is a second peak in the pulse height distribution, centered at twice the value (~74 mV) of the center of the first peak (~37 mV). The theoretical expression for the pulse height distribution for the VLPC is given by the gamma distribution[9]

$$P(M)=\frac{1}{M}\left(\frac{1}{F-1}\frac{M}{\langle M\rangle}\right)^{1/(F-1)}\frac{\exp\left(-\frac{1}{F-1}\frac{M}{\langle M\rangle}\right)}{\Gamma\left(\frac{1}{F-1}\right)}, \tag{1}$$

where M is the statistical variable that describes the multiplication gain, $\langle M\rangle$ is the average of M, and $F=\langle M^2\rangle/\langle M\rangle^2$ is

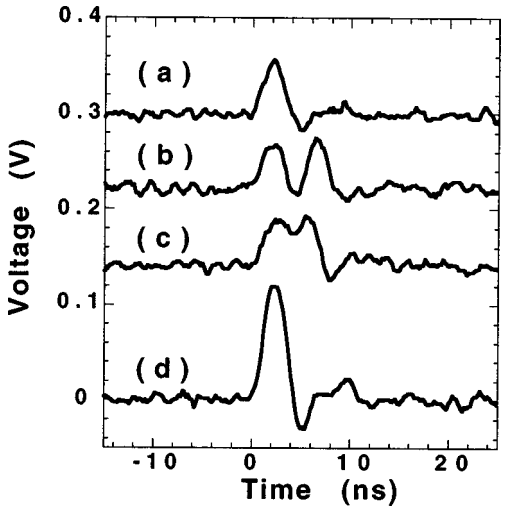

FIG. 2. Real-time trace of photon detection signal recorded by a 5 GS/s digitizing oscilloscope. The time delay between the two beams is changed by modifying the optical path length. The traces are shifted vertically for clarity. (a) Single-photon detection signal. (b) 5 ns delay. (c) 3 ns delay. (d) Zero delay.

the excess noise factor (ENF) for the multiplication process. From the pulse height distribution obtained in the experiment, we can calculate the mean ($\langle M\rangle$) and ENF (F) of the gain, and use these values in Eq. (1) to generate the dotted lines of Fig. 3. For Fig. 3(b), the mean two curves were generated separately to fit each peak, which were then added to give the dotted line shown. The excess noise factor deduced from these pulse height distribution was 1.026 for the single-photon pulse height distribution [in both Figs. 3(a) and 3(b)] and 1.012 for two-photon pulse height distribution, indicating almost noise-free avalanche multiplication. The bit-error rate P_e for distinguishing a two-photon detection event from a single-photon detection event is given by

$$P_e=\min_{V_T}\left\{\int_{V_T}^{\infty}P_1(V)dV+\int_{-\infty}^{V_T}P_2(V)dV\right\}, \tag{2}$$

where $P_1(V)$ and $P_2(V)$ are the normalized pulse height distribution for single-photon detection events and two-photon detection events, respectively, and V_T is the threshold voltage used for the discrimination. From the two distributions given in Fig. 3(b), P_e is minimized to 0.63% when V_T is chosen at ~54 mV. It should be noted that the discriminator level V_T for two-photon detection and the bit-error rate P_e can change slightly depending on the relative size of the two peaks in Fig. 3(b).

The narrow bandpass filter used in front of the VLPC had transmittance of about 50% at 702 nm, and such one photon optical loss is responsible for the small two-photon detection peak compared to the single-photon detection peak. The net quantum efficiency for two-photon detection can be estimated if such optical loss is subtracted. We used two single photon counting modules [(SPCMs); single photon counting detectors based on avalanche photodiodes] to characterize the optical loss and the quality of the two-photon source. Large area (500 μm diameter) APDs are employed in our SPCMs, and the quantum efficiency of these detectors are ~50±5% near the measurement wavelength of 702 nm. We placed two SPCMs at locations A and B indicated in Fig.

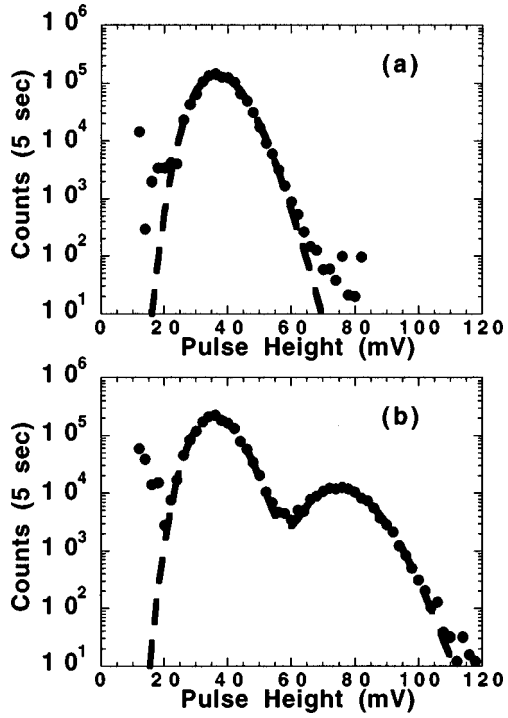

FIG. 3. Pulse height distribution for the detected photons. Counts were integrated for 5 s at each point. The dark circles are experimental data, and the dotted lines are theoretical fits using Eq. (1). (a) Single beam input. (b) Two beam input with zero time delay between the two beams.

1 with narrow bandpass filters in front of each detector and measured the single photon count rates of two beams [A and B, in units of counts per second (cps)] independently, and the coincidence count rate of the two beams (C). Given the dark counts of the SPCMs (which is measured by blocking the input beams) and the quantum efficiency, we can estimate the net photon flux at the SPCM inputs (A_0 and B_0) and the net coincidence input (C_0) (Table I). These three numbers characterize the one photon loss rate of the two-photon source made up of a parametric down converter and all the optical components used, including the narrow bandpass filters.

Once these properties are known, we can estimate the two-photon detection efficiency of the VLPC. The ratio of the two-photon detection events and single-photon detection events is given by

$$\frac{R_2}{R_1}=\frac{\eta_2 C_0}{\eta_1(A_0+B_0-2\eta_1 C_0)+D_0}, \tag{3}$$

where R_1 and R_2 denote the single- and two-photon count rates, η_1 and η_2 denote the single- and two-photon detection quantum efficiency, and D_0 denotes the dark count rate of the VLPC. Independent measurements at the same operating conditions yield the values $\eta_1=70\pm5\%$ and $D_0=1.7\times10^4$ cps for the single-photon detection quantum efficiency and the dark count rate, respectively. Single-photon detection quantum efficiency η_1 was degraded by about 5% because of saturation effect caused by a relatively large input photon flux ($\sim5.6\times10^5$ cps) used in the experiment.[5] The experimental value for R_2/R_1 can be found from integrating the pulse height distribution curve in Fig. 3(b), and is found to be 8.5×10^{-2}. Using these data with the values for A_0, B_0, and C_0 in Table I, we can deduce the two-photon detection quantum efficiency $\eta_2=47\%$. The maximum value expected for a two-photon detection quantum efficiency is given by $\eta_{2,\max}=\eta_1^2=49\%$, and the two-photon detection quantum efficiency in our setup is limited by the single-photon detection quantum efficiency within the measurement accuracy.

TABLE I. Count rates, dark count rates, and coincidence count rates for the two-photon source using SPCM detectors. All numbers are given in units of counts per second (cps).

Quantity	Measured counts	Dark counts	Net counts
A	1.22×10^5	2.59×10^3	2.38×10^5 (A_0)
B	8.41×10^4	1.37×10^4	1.41×10^5 (B_0)
C	1.13×10^4	negligible	4.53×10^4 (C_0)

In conclusion, we report here a photon detector based on VLPC that can distinguish between a single-photon incidence and two-photon incidence with high quantum efficiency (47%), good time resolution (2 ns), and low bit-error rate ($\sim0.63\%$). The performance of the detector was tested quantitatively using a two-photon source employing twin photons generated by a degenerate parametric down-conversion process.

J. Kim wants to thank Dr. S. Machida of NTT Basic Research Labs for helpful discussion on the electronic circuits. This work was partly supported by JSEP.

[1] H. Dautet, P. Deschamps, B. Dion, A. D. MacGregor, D. MacSween, R. J. McIntyre, C. Trottier, and P. P. Webb, Appl. Opt. **32**, 3894 (1993).
[2] M. D. Petroff, M. G. Stapelbroek, and W. A. Kleinhans, Appl. Phys. Lett. **51**, 406 (1987).
[3] M. Atac, J. Park, D. Cline, D. Chrisman, M. Petroff, and E. Anderson, Nucl. Instrum. Methods Phys. Res. A **314**, 56 (1992).
[4] A. Peacock, P. Verhoeve, N. Rando, A. van Dordrecht, B. G. Taylor, C. Erd, M. A. C. Perryman, R. Venn, J. Howlett, D. J. Goldie, J. Lumley, and M. Wallis, Nature (London) **381**, 135 (1996).
[5] S. Takeuchi, J. Kim, Y. Yamamoto, and H. H. Hogue, Appl. Phys. Lett. (to be published).
[6] P. G. Kwiat, Phys. Rev. A **52**, 3380 (1995).
[7] S. L. Braunstein and H. J. Kimble, Nature (London) **394**, 840 (1998); D. Bouwmeester, J.-W. Pan, M. Daniell, H. Weinfurter, M. Zukowski, and A. Zeilinger, *ibid.* **394**, 841 (1998).
[8] T. P. Spiller, Proc. IEEE **84**, 1719 (1996).
[9] G. B. Turner, M. G. Stapelbroek, M. D. Petroff, E. W. Atkins, and H. H. Hogue, in *SciFi 93-Workshop on Scintillating Fiber Detectors*, edited by A. D. Bross, R. C. Ruchti, and M. R. Wayne (World Scientific, New Jersey, 1993), p. 613; M. G. Stapelbroek and M. D. Petroff, *SciFi 93-Workshop on Scintillating Fiber Detectors* (World Scientific, New Jersey, 1993), p. 621.
[10] R. S. Bondurant, P. Kumar, J. H. Shapiro, and M. M. Salour, Opt. Lett. **7**, 529 (1982).
[11] P. G. Kwiat, A. M. Steinberg, R. Y. Chiao, P. H. Eberhard, and M. D. Petroff, Phys. Rev. A **48**, R867 (1993).
[12] N. G. Woodard, E. G. Hufstedler, and G. P. Lafyatis, Appl. Phys. Lett. **64**, 1177 (1994).
[13] R. J. McIntyre, IEEE Trans. Electron Devices **ED-13**, 164 (1966).
[14] J. Kim, Y. Yamamoto, and H. H. Hogue, Appl. Phys. Lett. **70**, 2852 (1997).
[15] S. Takeuchi, Meeting Abstracts of the Phys. Soc. of Japan **53**, 292 (1998).